Transonic Wing Flows Using an Euler/Navier-Stokes Zonal Approach

Terry L. Holst*
NASA Ames Research Center, Moffett Field, California
Unver Kaynak†
Stanford University, Stanford, California
Karen L. Gundy‡
NASA Ames Research Center, Moffett Field, California
Scott D. Thomas‡
Sterling Software, Palo Alto, California
and
Jolen Flores‡ and Neal M. Chaderjian‡
NASA Ames Research Center, Moffett Field, California

Transonic flowfields about wing geometries are computed using an Euler/Navier-Stokes approach in which the flowfield is divided into several zones. Wind-tunnel wall effects are modeled easily and accurately with the new grid-zoning algorithm because the wind-tunnel grid is constructed as an exact subset of the corresponding free-air grid. Solutions are obtained that are in good agreement with experiment, including cases with significant wind-tunnel wall effects and shock-induced separation on the upper wing surface.

Introduction

THE fields of computational fluid dynamics (CFD) and computer hardware have been rapidly advancing over the last decade. It is now possible to demonstrate the importance of CFD in the field of aircraft design and performance prediction for general flow conditions. The problem of solving the Euler/Navier-Stokes equations about reasonably complete aircraft configurations needs to be undertaken, and significant results need to be produced and disseminated which demonstrate the power of this approach.

In this paper, Navier-Stokes solutions for the transonic flow over an isolated-wing geometry with both free-air and wind-tunnel wall boundary conditions are presented. The resulting computer code, called TNS (Transonic Navier-Stokes), utilizes a zonal approach with a total of four grid zones. The Euler equations are solved in the two outer zones, and the thin-layer Navier-Stokes equations are solved in the two inner zones near the wing surface. An H-mesh topology is used in both directions (chordwise and spanwise) and allows a rather unique capability with regard to the wind-tunnel wall simulation. The wind-tunnel wall grid is computed as an exact subset of the free-air grid. The free-air grid has the same inflow and outflow as the wind-tunnel wall grid, but extends above and below the wind-tunnel wall grid surfaces. Thus, any grid errors caused by going from the wind-tunnel wall grid to the free-air grid are removed. This is not the case with wind-tunnel wall calculation procedures that use C- or O-mesh topologies.

Presented as Paper 85-1640 at the AIAA 18th Fluid Dynamics and Plasmadynamics and Lasers Conference, Cincinnati, OH, July 16-18, 1985; received March 7, 1986; revision received Aug. 8, 1986.

*Chief, Applied Computational Fluids Branch. Associate Fellow AIAA.
†Graduate Student. Student Member AIAA.
‡Research Scientist. Member AIAA.

Governing Equations and Numerical Algorithm

The basic governing equations and the numerical algorithm have been taken from the Pulliam-Steger ARC3D computer code.[1,2] The equations solved in this study are the Reynolds-averaged Navier-Stokes equations written in strong conservation-law form. These equations are simplified by using the standard thin-layer approximation for the viscous terms. For zones in which viscous effects are not important, the Euler equations are used. By using the Euler equations over a significant part of the flow domain, the efficiency of the calculation procedure is improved. Information about the numerical algorithm and how it is affected by the present zonal scheme is discussed by Flores.[3] Additional key elements of the present work, including the zonal interface algorithm and the overall computer code memory management scheme, are discussed by Holst et al.[4]

The basic numerical algorithm used by the TNS computer code is a diagonalized, ADI-type algorithm due to Pulliam and Chaussee,[5] which solves a set of five scalar pentadiagonal matrices along each coordinate direction. This scheme uses a standard second-order-accurate central differencing of the governing equations, a fourth-order-accurate smoothing operator on both the left- and right-hand sides of the iteration scheme, and a spatially varying time step based on Jacobian scaling. The Baldwin-Lomax algebraic turbulence model[6] is used in the present study for all of the calculations. This model is used because it is easy to implement.

Zonal Approach

Grid Generation

The grid-generation process begins with the generation of a single-zone base grid which includes the entire flowfield. This grid contains no viscous clustering and has an H-mesh topology in both the spanwise and chordwise directions. It can be generated from either of two approaches: the elliptic solver approach of Sorenson[7] or the parabolic solver approach of Edwards.[8] Both of these approaches solve partial differential equations in order to generate smooth, well-

behaved, finite-difference meshes. They have the capability of generating suitable grids about isolated wing geometries with either free-air or wind-tunnel wall outer boundaries.

Once the base grid is generated, a zoning algorithm is used to divide the grid into separate zones. The first grid zone (grid 1) is the base grid itself, with a small block of grid points near the wing removed. The second grid zone (grid 2) basically occupies the space left open by the block of points removed from grid 1 with a small region of overlap included (usually one or two grid cells on all boundaries). Grid 2 is constructed so as to contain twice as many grid points in each spatial direction as the original base grid. This refinement of grid 2 relative to the base grid is accomplished using cubic-spline interpolation. Similar to grid 1, grid 2 has a small block of points removed near the wing.

The final two grid zones (grids 3 and 4) occupy the space left open by the block of points removed from grid 2, again with a small region of overlap included. Grids 3 and 4 are constructed so as to contain the same number of points in both the spanwise and chordwise directions as grid 2. However, the grid points in the normal direction are highly clustered in order to capture viscous effects on the wing surfaces. Grid 3 is designed to capture the upper-wing-surface viscous effects, and grid 4 the lower-wing-surface viscous effects. The two outer inviscid grid zones are topologically represented in the computational domain as cubes with smaller cubes removed from the middle. The third and fourth viscous zones are topologically represented as simple cubes in the computational domain. This grid topology can be more adequately explained through an example.

Figure 1 shows a typical grid with outer boundary positions specified to coincide with the position of the wind-tunnel walls from the Ames High Reynolds Number Channel I.[9] The grid is plotted in perspective so that detail on the upper and lower wind-tunnel wall surfaces, the inflow and outflow planes, and the wing symmetry plane are all visible. This grid, which is generated directly by the parabolic grid-generation approach, becomes the outer, coarse grid zone (grid 1). The grid detail near the wing symmetry-plane juncture has been removed. Grid zones 2–4 are located in this region. An expanded view of the grid in the vicinity of the wing showing detail of grid zones 2–4 is shown in Fig. 2. The wing geometry used in this case is composed of NACA 0012 cross sections, has a taper ratio (TR) of 1.0, 20 deg of leading edge sweep, an aspect ratio of 3.0, and is rigged in the wind-tunnel wall grid at an angle of attack of 2 deg. This wing does not have any twist or dihedral. Note that the grids immediately adjacent to the wing surface (grid zones 3 and 4) are highly clustered in the normal direction and, therefore, are appropriate for a Navier-Stokes flow solver. Also note that the Navier-Stokes grids expand in thickness from the leading edge toward the trailing edge to better capture the growing boundary layer. Figure 3 shows a perspective view of the grid with the symmetry plane and wing surface highlighted. From this view, the wing-surface grid resolution, including treatment of the wingtip, can be seen.

The total number of grid points used in the grid of Figs. 1–3 is 149,071. The individual grid point breakdown for each zone is as follows: grid 1, $65\times20\times19=24{,}700$; grid 2, $69\times29\times21=42{,}021$; grid 3, $61\times27\times25=41{,}175$; and grid 4, $61\times27\times25=41{,}175$. This grid has been constructed to fit the geometry used in the experiment of Lockman and Seegmiller.[9] Another grid with exactly the same characteristics for zones 2–4, but with free-air boundaries specified for grid zone 1, has also been generated. The free-air grid is constructed from the wind-tunnel wall grid by simply adding several grid surfaces to the top and bottom boundaries of the wind-tunnel wall grid and to the side-wall boundary outboard of the wingtip. Therefore, the wind-tunnel wall grid is an exact subset of the free-air grid. The grid immediately surrounding the wing geometry, including the inflow and outflow boundary positions, is exactly the same in both the free-air and wind-tunnel wall grids. The number of points in the free-air grid (166,621) is slightly larger than that in the wind-tunnel wall grid because grid zone 1 is slightly larger: $65\times26\times25=42{,}250$.

Since the free-air and wind-tunnel grids are identical in the vicinity of the wing, computed flow for the same conditions on both grids must be free of grid-induced perturbations near the wing. Any differences between the free-air and wind-tunnel wall cases must be attributable to changes in the outer-zone grid and to the use of different outer boundary conditions. This represents a better way of simulating wind-tunnel wall interference than approaches requiring the generation of two grids, which can be drastically different in the vicinity of the wing. This point is especially important when the wind-tunnel walls are close to the model being tested.

Data Management

Once the grid is generated and divided into the proper zones, the flow solver is initiated. The iteration procedure

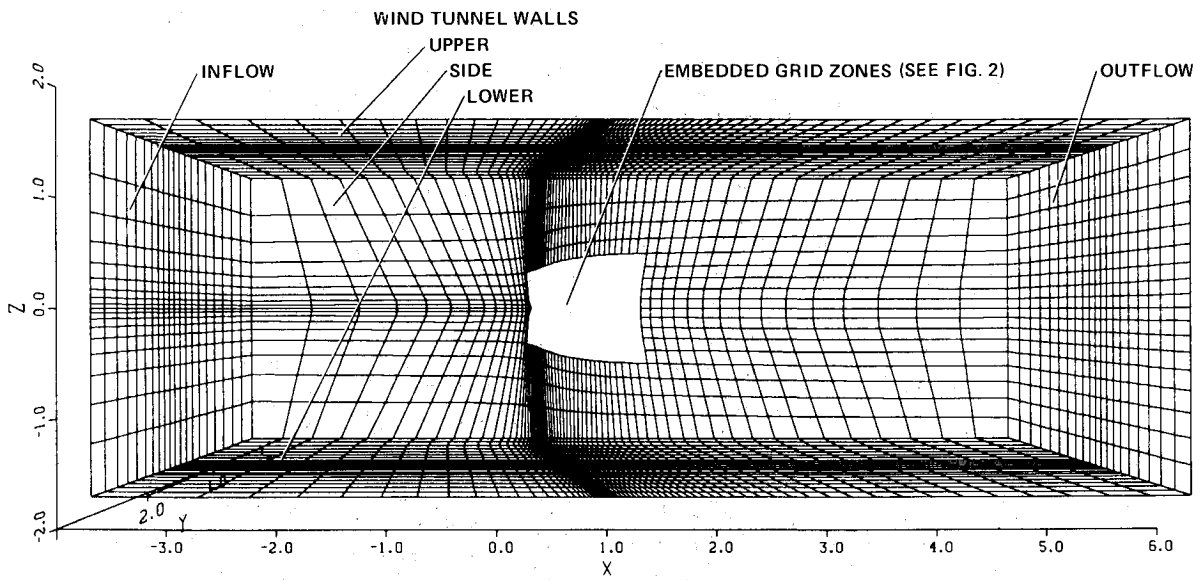

Fig. 1 Typical finite-difference grid showing detail on wind-tunnel walls.

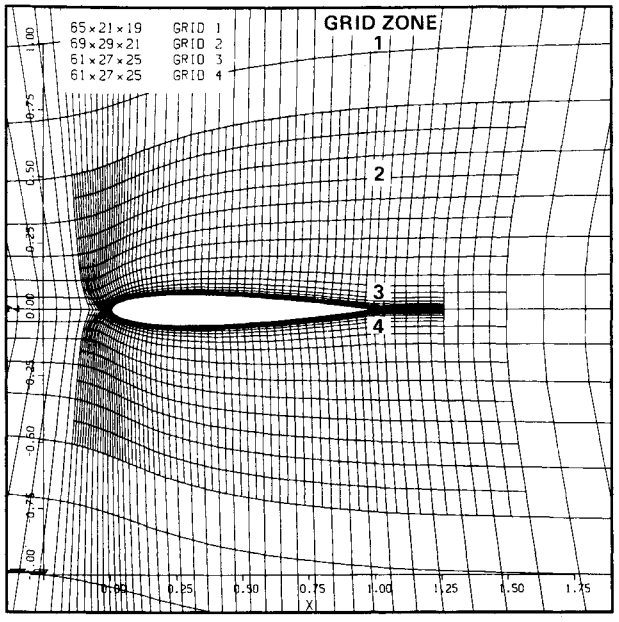

Fig. 2 Blowup of embedded grid near wing geometry.

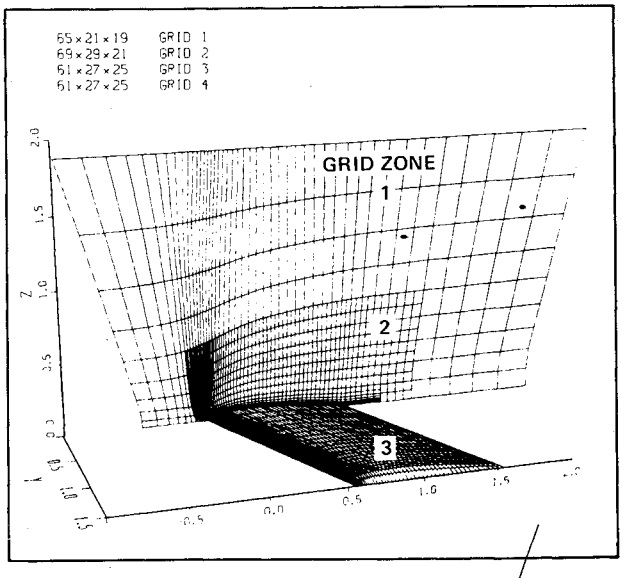

Fig. 3 Perspective view of embedded grid with upper symmetry plane ($y=0$, $z\geq 0$) and wing surface highlighted.

starts in the outer Euler block (grid 1), proceeds to the inner Euler block (grid 2), and ends with the two Navier-Stokes blocks; first the upper block (grid 3), and then the lower block (grid 4). Only one iteration using a spatially varying time step is completed in each grid zone before passing to the next.

Only the flowfield solution, transformation Jacobian, and the turbulence model arrays (when appropriate) associated with a single block reside in main memory. The information associated with the other blocks resides in extended storage. In the present zonal approach, the use of extended storage allows a great deal of flexibility, since a larger number of grid blocks can be supported without significant additions to main memory. The current version of the TNS code, with grid dimensions as outlined previously in the grid-generation section, requires 5.8 million words of storage. All extended-storage arrays are stored in 64-bit precision, with the exception of the metric arrays, which are stored with 32-bit precision. A test was performed with 64-bit metric storage that

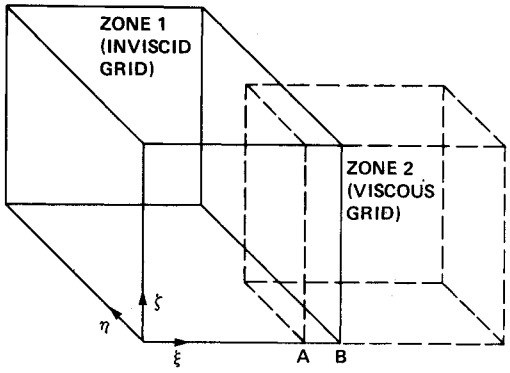

a) Two-zone arrangement showing overlap.

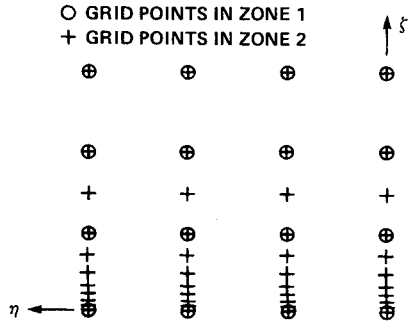

b) Grid point detail in the overlap region ($\xi = A$ plane).

Fig. 4 Grid zone interface procedure.

produced results very close to those of the case with 32-bit metric storage.

To allow more space in main memory, the metrics are shuffled into main memory from extended storage in two-dimensional planes as needed. This allows the maximum grid size for each grid zone to be about 50,000 points for every million words of main memory used. Because the flow-solver algorithm used in TNS is an ADI-type algorithm with implicit sweeps in all three directions, the metrics must be transferred into main memory with three different orientations: *x-y*, *x-z*, and *y-z* planes. Thus, there are three different copies of the metrics stored on the extended-storage device corresponding to the three different metric orientations.

A typical solution computed with the TNS computer code involving about 150,000 grid points requires about 500 iterations to reduce the L_2 norm of the residuals in each grid zone by about three orders of magnitude. During this typical run, 5.97 billion 64-bit words are transferred between main memory and extended storage. This requires about 2780 s of CPU time on the Cray XMP computer and about 40 s of I/O time. Additional computational details associated with the TNS computer code are reported in Ref. 10.

Zonal Interface Scheme

Communication between neighboring blocks is achieved by means of an interpolation procedure. The grid zones are constructed to overlap by a specific number of cells, usually one or two. Then, information required at the boundary of one zone is interpolated from the interior of another zone. Because the grid zones are carefully constructed from a base grid such that surfaces requiring interpolation are coincident, the interpolation is greatly simplified. The most complicated zonal interface boundary condition involves only a series of one-dimensional linear interpolations. This situation is illustrated in Fig. 4. In this hypothetical case, grid zone 1 is an inviscid grid that interfaces with grid zone 2, a highly stretched viscous grid (see Fig. 4a). The idea is to obtain flowfield information from the interior of zone 1 and use it

to satisfy the proper conditions on the $\xi = A$ plane of zone 2. Since the grids of zones 1 and 2 both have been constructed to coincide with plane $\xi = A$, this process is greatly simplified. A blowup of this $\xi = A$ interface plane is shown in Fig. 4b. Note that the points from both grid zones are shown, and that the grid points from grid zone 1 represent a subset of the grid zone 2 points. Thus, the interpolation between zones is just a series of one-dimensional interpolations along the ζ direction.

The process of interpolating information back from zone 2 to zone 1, which is required for the $\xi = B$ interface plane, is even simpler than in the first case because the interpolation becomes simple "injection." Even though interpolation is carried out, the end result of this operation is the straight transfer of values from zone 2 to zone 1 without interpolation errors. Every grid point in the zone 1 ($\xi = B$) boundary has an exactly matching point in the zone 2 ($\xi = B$) boundary. This is readily seen by looking at Fig. 4b and noting that every zone 1 point (circular symbols) has an exact matching zone 2 point (plus symbols).

Computed Results

Turbulence Model Validation

In order to validate the TNS computer code and, in particular, the coding of the Baldwin-Lomax turbulence model, a simple nonlifting case is presented first. This case involves a subcritical flow ($M_\infty = 0.5$) about a large-aspect-ratio wing composed of NACA 0012 airfoil sections. Because of the large-aspect-ratio characteristic, the symmetry plane solution is essentially two-dimensional and should compare favorably with two-dimensional results. Such a comparison is shown in Fig. 5. The pressure coefficient distributions from TNS and TRIVIA (a transonic airfoil code with viscous corrections[11]) are compared with experimental data taken from Ref. 12. The agreement for this easy case is excellent. In particular, note the smooth leading-edge pressure gradient obtained from TNS. The H-mesh singularity does not cause any problems for this calculation.

Velocity profiles obtained from the TNS and TRIVIA codes are compared at several airfoil chordwise stations in Fig. 6. The agreement is generally quite good. The discrepancies that do exist are probably caused by differences in grid resolution. The TNS results at chordwise stations $x/c = 0.18$ and 0.97 have 15 and 21 grid points in the boundary layer, respectively. The boundary-layer results have a constant 50 points for every chordwise station. The y^+ value (in law-of-the-wall terminology) at the first grid point off the wing surface for the TNS results is about 2–4. For the TRIVIA results, the corresponding y^+ values are about 1–2. Nevertheless, the present results seem to substantiate that the Baldwin-Lomax turbulence model is correctly coded.

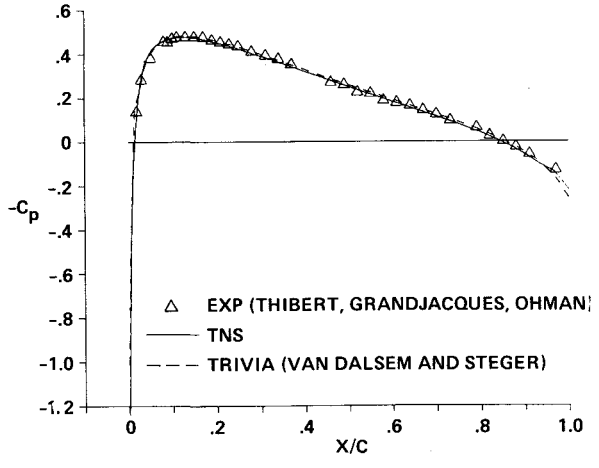

Fig. 5 Pressure coefficient comparisons (NACA 0012 airfoil section, $\Lambda = 0$ deg, large aspect ratio, TR = 1.0, $M_\infty = 0.5$, $\alpha = 0$ deg, $Re = 3 \times 10^6$).

Nonlifting Supercritical Case

The next solution involves a transonic flowfield about an NACA 0012 wing with an aspect ratio of 3.0, a taper ratio of 1.0, 20 deg of sweep, a Reynolds number based on chord of 8

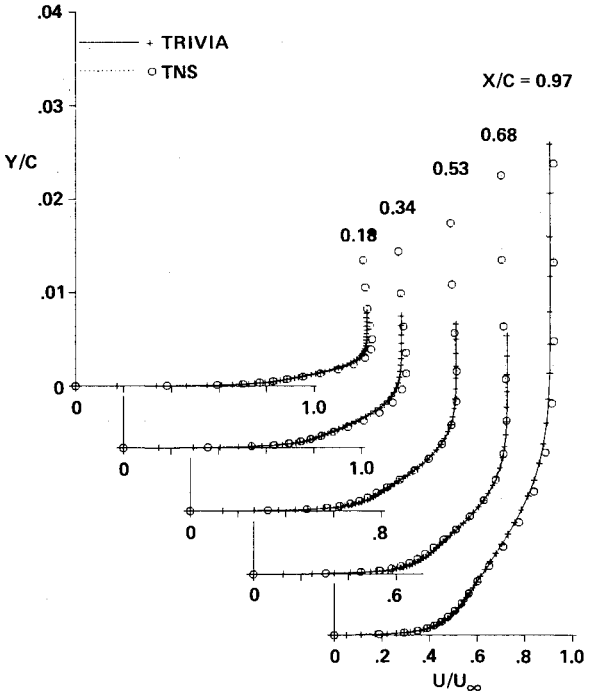

Fig. 6 Boundary-layer velocity profile comparisons (NACA 0012 airfoil section, $\Lambda = 0$ deg, large aspect ratio, $M_\infty = 0.5$, $\alpha = 0$ deg).

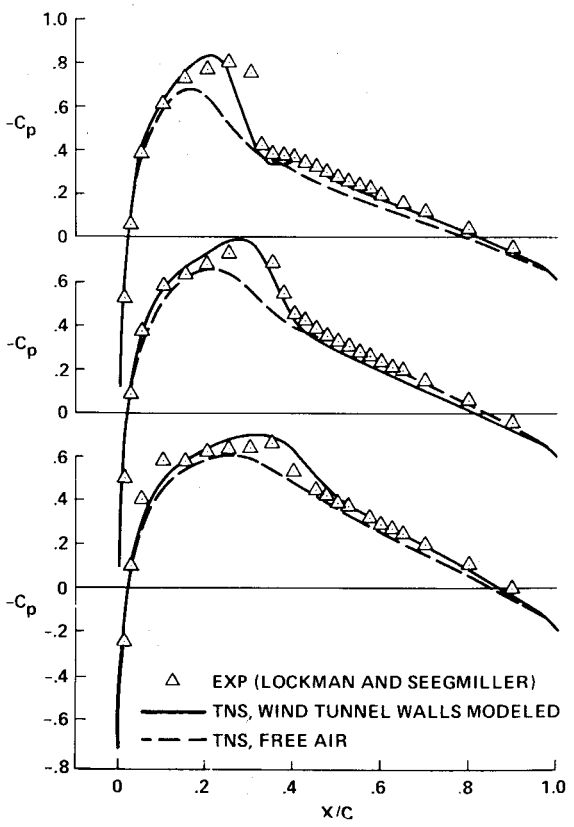

Fig. 7 Pressure coefficient comparisons (NACA 0012 airfoil section, $\Lambda_{LE} = 20$ deg, $AR = 3.0$, TR = 1.0, $M_\infty = 0.795$, $\alpha = 0$ deg, $Re = 8 \times 10^6$).

million, and a freestream Mach number of 0.795. This wing has no twist or dihedral and is nonlifting. The grid used for this calculation is very similar to the grid previously presented in Figs. 1–3 (except the angle of attack for the present case is zero). The wind-tunnel walls are solid (not slotted or porous) and are slightly less than 2 chords above and below the wing. Numerical results compared with the experimental results of Lockman and Seegmiller[9] are now presented.

Pressure coefficient distributions at several spanwise locations are compared in Fig. 7. For this case, the wind-tunnel walls significantly influence the flowfield physics. This is readily seen from Fig. 7 by comparing the free-air and wind-tunnel-wall computed solutions with experiment. The results obtained with the wind-tunnel walls modeled are in better agreement with experiment than the free-air results. For this calculation, a weak shock exists across the wing and is captured quite successfully.

Lifting Supercritical Case

The next case involves the same geometry as the previous one at a freestream Mach number of 0.826 and an angle of attack of 2 deg. For this case, the wind-tunnel-wall effects are more significant. This can be seen in Fig. 8 where the pressure coefficient distributions from TNS, with and without the walls modeled, are compared with experiment. The shift in shock position caused by the tunnel walls is obvious. The shock position for the case with walls is in good agreement with the experimental shock position, while the free-air shock position is too far upstream by about 10–12% of chord.

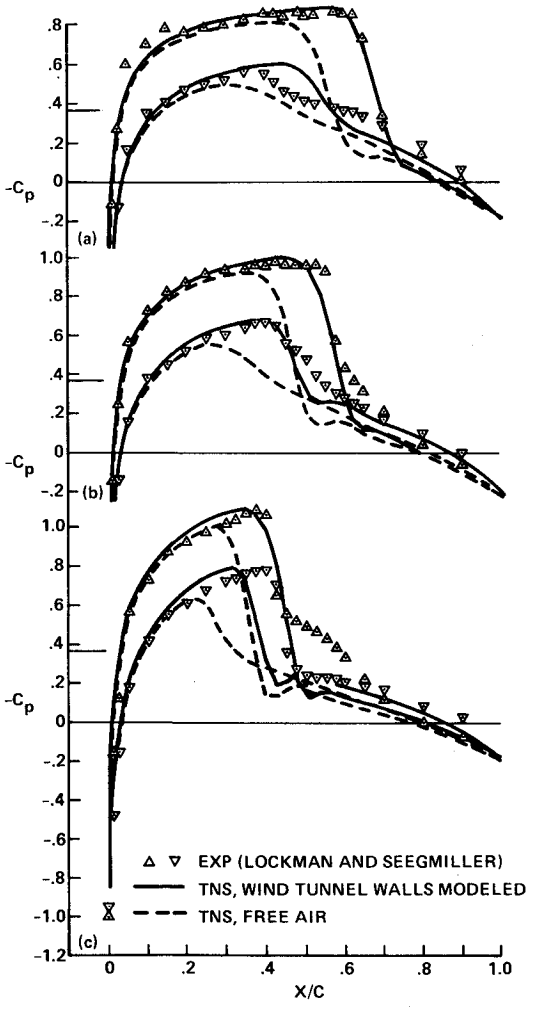

Fig. 8 Pressure coefficient comparisons (NACA 0012 airfoil section, $\Lambda_{LE}=20$ deg, $AR=3.0$, TR = 1.0, $M_\infty=0.826$, $\alpha=2$ deg, $Re=8\times10^6$). a) $2y/b=0.25$; b) $2y/b=0.50$; c) $2y/b=0.78$.

General agreement between the wind-tunnel wall case and experiment is better inboard of mid-semispan than it is outboard. In particular, the computed upper-surface shock strength at $2y/b=0.78$ is larger than that of the experiment. This is caused by a large boundary-layer separation in the experimental results at this semispan location that is not accurately reproduced by the computed results. A good picture of this situation is given in Figs. 9 and 10, which show a set of computed particle paths (Fig. 9) and an oil-flow photograph taken from the experiment (Fig. 10). The spanwise extent of the experimental separation is reasonably predicted by the computation, but the streamwise extent is underpredicted. Note that the Mach number on the oil flow ($M_\infty=0.828$) is slightly higher than that of the original experimental pressure distribution run ($M_\infty=0.826$). Oil-flow results at lower Mach numbers ($M_\infty=0.816$) indicate that the flow pattern is quite sensitive to changes in freestream Mach number. This may have an impact on the difference in the relative sizes of the

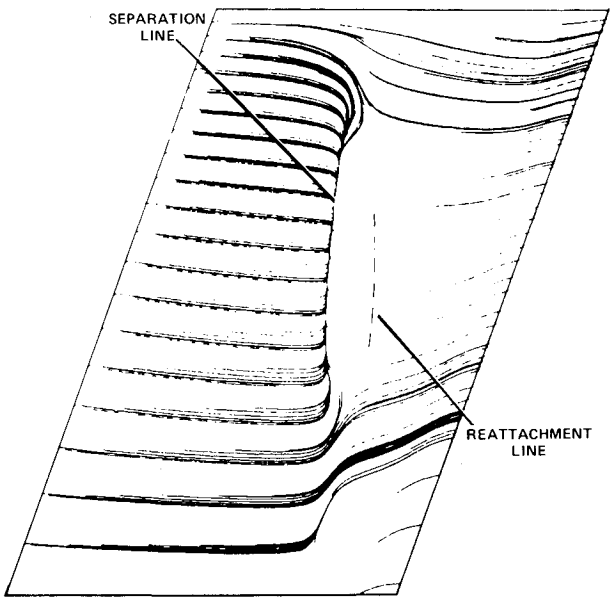

Fig. 9 Computed particle paths on the upper wing surface (NACA 0012 airfoil section, $\Lambda_{LE}=20$ deg, $AR=3.0$, TR = 1.0, $M_\infty=0.826$, $\alpha=2$ deg, $Re=8\times10^6$).

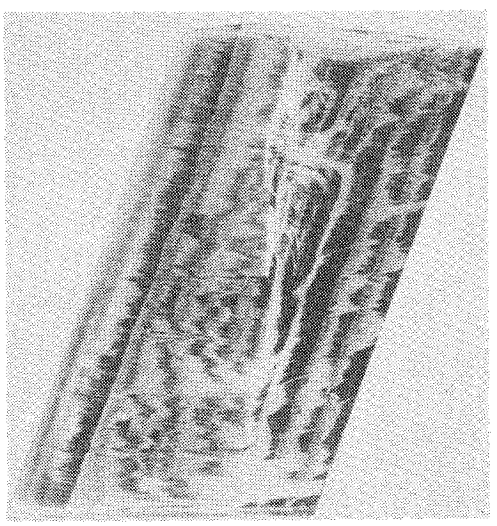

Fig. 10 Oil-flow pattern on upper wing surface (from Lockman and Seegmiller[9]) (NACA 0012 airfoil section, $\Lambda_{LE}=20$ deg, $AR=3.0$, TR = 1.0, $M_\infty=0.828$, $\alpha=2$ deg, $Re=8\times10^6$).

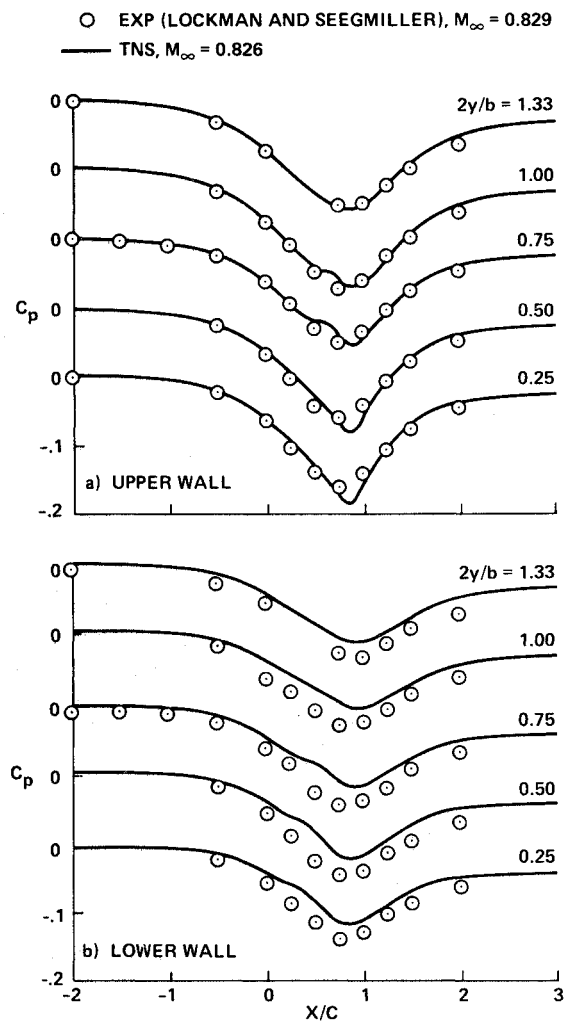

Fig. 11 Pressure coefficient comparisons on the wind-tunnel walls (NACA 0012 airfoil section, $\Lambda_{LE} = 20$ deg, $\mathcal{R} = 3.0$, TR = 1.0, $M_\infty = 0.826$, $\alpha = 2$ deg, $Re = 8 \times 10^6$).

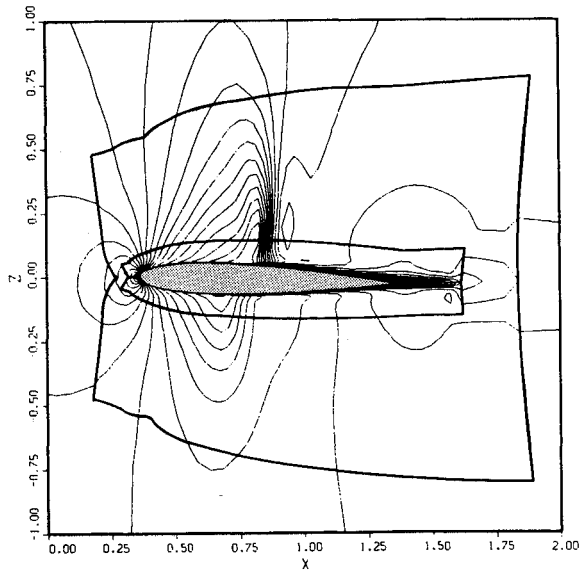

Fig. 12 Cross-sectional Mach number contours (NACA 0012 airfoil section, $\Lambda_{LE} = 20$ deg, $\mathcal{R} = 3.0$, TR = 1.0, $M_\infty = 0.826$, $\alpha = 2$ deg, $Re = 8 \times 10^6$, $2y/b = 0.66$).

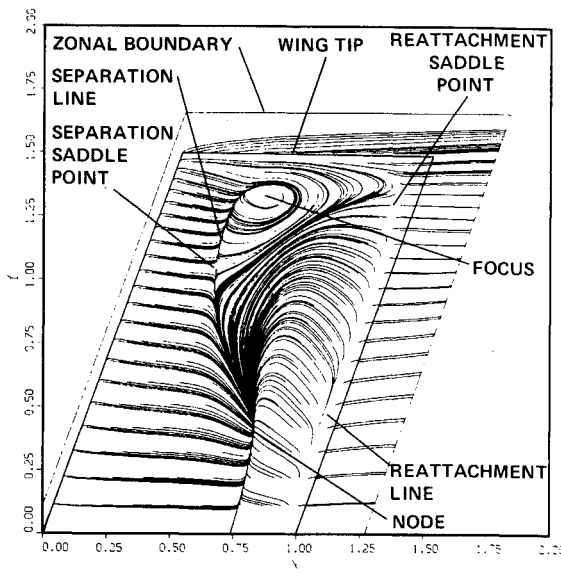

Fig. 13 Computed particle paths on the upper wing surface (NACA 0012 airfoil section, $\Lambda_{LE} = 20$ deg, $\mathcal{R} = 3.0$, TR = 1.0, $M_\infty = 0.9$, $\alpha = 5$ deg, $Re = 8 \times 10^6$).

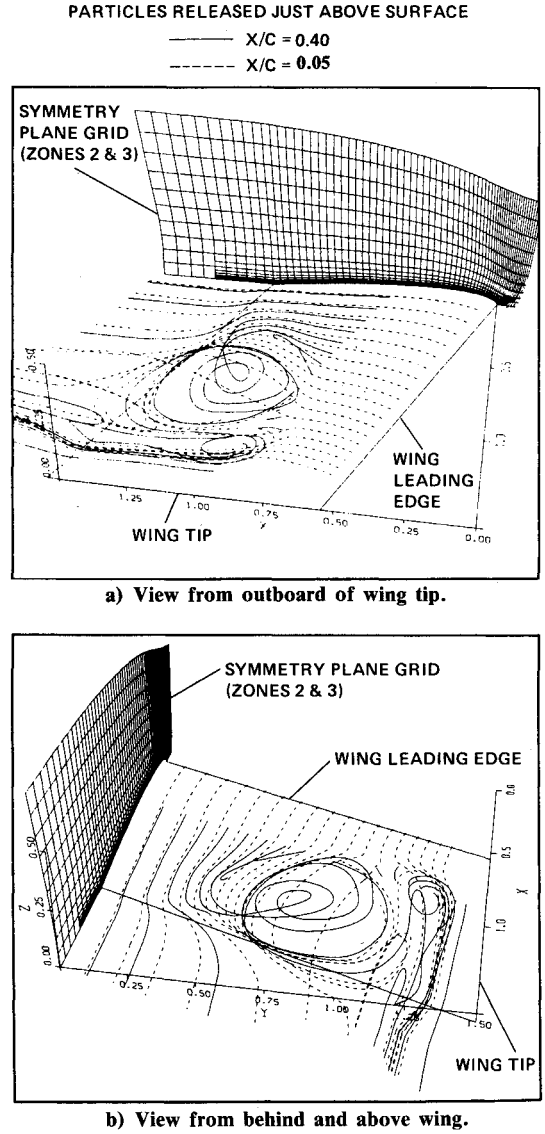

Fig. 14 Computed three-dimensional particle paths on the upper wing surface (NACA 0012 airfoil section, $\Lambda_{LE} = 20$ deg, $\mathcal{R} = 3.0$, TR = 1.0, $M_\infty = 0.9$, $\alpha = 5$ deg, $Re = 8 \times 10^6$).

computed and experimental separation zones. In addition, coarse-grid and turbulent model effects probably cause some of the disagreements in the separated region.

Despite the difference in the size of the separation zone, the overall comparison in Figs. 9 and 10 is quite encouraging. The computed position of the separation is in good agreement with experiment, as are many other qualitative details of the flowfield. In particular, the influence of the tip vortex forcing the flow inboard over the last half of chord at the tip is almost identically reproduced by the computation. The deflection of flow lines at about half-chord for the inboard semispan stations is apparent for both the computation and the experiment. This is probably caused by the shock wave, which cuts across the wing at about this position. Finally, the beginning of the formation of surface vortices at each end of the separation zone is also apparent in both results. These vortices are counter-rotating and form a very interesting flow pattern, especially as the Mach number is increased.

Both the computed and measured pressures on the upper and lower wind-tunnel walls are displayed in Fig. 11. The agreement between the two results on the upper wind-tunnel wall is excellent, while for the lower wall it is good. The computed pressure coefficient one chord downstream of the wing ($x/c=2$) is higher than the experimental value by about 0.02. This may indicate that the tunnel flow is not fully returning to freestream conditions downstream of the wing. Such a situation could affect the results obtained and will be investigated in the future.

Figure 12 is the final result presented for the $M_\infty=0.826$ case and consists of Mach number contours plotted in a wing cross-sectional plane at a span station of $2y/b=0.66$. The zonal boundaries are also shown in this plot. Note the smoothness with which the shock wave crosses the zonal interface boundary. This indicates that this interface is being implemented in a conservative manner. In addition, most of the other contours cross the zonal interface boundaries in a smooth and continuous fashion. Downstream in the wake, where the fine viscous grid interfaces with a relatively coarse inviscid grid (see Fig. 2), the wake abruptly stops. This aspect of the solution exists because the coarse inviscid grid cannot retain the sharp gradient detail of the viscous wake. If this portion of the solution were important, a separate grid zone could easily be added to capture the viscous wake.

Massive Shock-Induced Boundary-Layer-Separation Case

The last solution presented consists of a massive, shock-induced boundary-layer separation. This case was computed to ascertain the degree of robustness of the present algorithm and, in particular, the ability of the present zonal interface scheme to cope with large flow gradients. The geometry used is the same as that of the last two cases. The freestream Mach number and angle of attack have been arbitrarily chosen to be 0.9 and 5 deg, respectively. Utilization of the wind-tunnel wall boundaries, as described in Figs. 1-3, produced a "choked" solution with a shock wave spanning the tunnel. After several hundred iterations and a moderately converged calculation, the solution (as expected) diverged. This, of course, was a consequence of the "fixed" upstream boundary conditions forcing more mass flow through the tunnel than the choked condition would allow.

The solution was repeated with free-air boundary conditions, and then convergence was easily achieved. Computed particle paths on the upper wing surface are displayed in Fig. 13. Note that approximately half of the upper wing surface is separated. The solution contains several interesting features, including a separation saddle point, a focus, a reattachment saddle point, and a node. Note also that this computed solution has a stable sequence of critical points on the separation line; that is, a node followed by a saddle point and then a focus (see Ref. 13).

Two different perspective views of the three-dimensional particle paths are shown in Fig. 14. Figure 14a shows a view

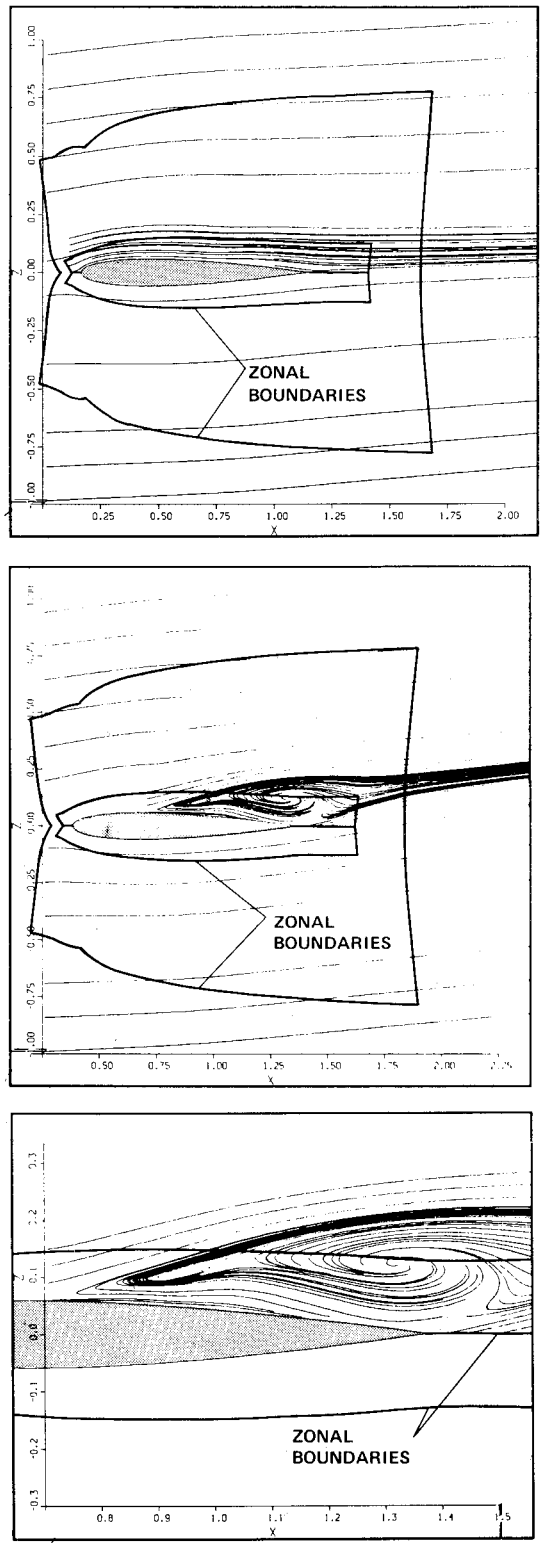

Fig. 15 Computed cross-sectional particle paths (NACA 0012 airfoil section, $\Lambda_{LE}=20$ deg, $AR=3.0$, TR = 1.0, $M_\infty=0.9$, $\alpha=5$ deg, $Re=8\times10^6$). a) $2y/b=0.17$; b) $2y/b=0.66$; c) $2y/b=0.66$, blowup of separated flow region.

from outboard of the wingtip, and Fig. 14b a view from behind and above the wing. The dashed and solid lines are particle paths created by "releasing" particles just above the wing surface at $x/c=0.05$ and 0.40, respectively. The height and three-dimensionality of the separation zone are apparent in these figures. The dashed particle paths move along the wing surface until the separation line is encountered, and then are deflected up over the separation bubble with a few of the

dashed paths captured by the primary swirling flow at the center of the wing. The solid-particle paths are more intimately involved with the two swirling pockets of flow and essentially serve to define those regions.

The position of the separation region relative to the zonal interface boundary is best displayed by plotting particle paths constrained to lie in spanwise cross-sectional planes. Two such plots are displayed in Fig. 15. Figure 15 shows cross-sectional particle paths for semispan stations of $2y/b = 0.17$ ($k = 5$) (Fig. 15a) and $2y/b = 0.66$ ($k = 13$) (Figs. 15b and 15c). The first station ($k = 5$) is close to the node, as shown in Fig. 13, and the second station ($k = 13$) is close to the separation saddle point. At $k = 5$, the separation region is small and does not approach the zonal boundary. However, at $k = 13$, the separation region is large and easily extends above the zonal boundary from the Navier-Stokes region into the Euler region. Nevertheless, the solution looks qualitatively reasonable. A blowup of the separated portion of the solution is shown in Fig. 15c. From this figure, it can be seen that the particle paths pass smoothly across the interface boundary with no function or slope discontinuities. Thus, despite the existence of a strong shear gradient across the explicitly updated interface boundary, the present approach is capable of predicting a stable solution reasonably free from interface boundary influence.

Concluding Remarks

Transonic flowfields about wing geometries have been computed using a new Euler/Navier-Stokes zonal approach. The results presented include cases with shock/boundary-layer interaction and wind-tunnel wall interference effects. The wind-tunnel wall interference effects have been modeled in a unique way so as to minimize the numerical effects of changing grids from the wind-tunnel wall to free-air cases. The present results have been computed efficiently, requiring less than 1 h of computer time for a relatively fine mesh (150,000 grid points), and compare favorably with experimental data, at both the wing and wind-tunnel wall surfaces.

An additional result has been obtained, which involves massively separated flow due to shock/boundary-layer interaction. For this calculation, interesting flowfield features have been predicted for the first time, including a separation saddle point, a node, a reattachment saddle point, and a focus.

Acknowledgments

The authors would like to thank Drs. T. Pulliam and J. Steger of NASA Ames and Prof. B. Cantwell of Stanford University for their numerous discussions during the course of this work. The second author acknowledges support from NASA Ames through Contract NCA2-OR745-309.

References

[1]Pulliam, T.H. and Steger, J.L., "Implicit Finite-Difference Simulations of Three-Dimensional Compressible Flow," *AIAA Journal*, Vol. 18, Feb. 1980, pp. 159–167.

[2]Pulliam, T.H., "Euler and Thin-Layer Navier-Stokes Codes: ARC2D, ARC3D," Notes for the Computational Fluid Dynamics Users' Workshop, The University of Tennessee Space Institute, Tullahoma, TN, March 1984.

[3]Flores, J., "Convergence Acceleration for a Three-Dimensional Euler/Navier-Stokes Zonal Approach," AIAA Paper 85-1495, July 1985.

[4]Holst, T.L., Kaynak, U., Gundy, K.L., Thomas, S.D., Flores, J., and Chaderjian, N.M., "Numerical Solution of Transonic Wing Flows Using an Euler/Navier-Stokes Zonal Approach," AIAA Paper 85-1640, July 1985.

[5]Pulliam, T.H. and Chaussee, D.S., "A Diagonal Form of an Implicit Approximate-Factorization Algorithm," *Journal of Computational Physics*, Vol. 39, Feb. 1981, pp. 347–363.

[6]Baldwin, B.S. and Lomax, H., "Thin-Layer Approximation and Algebraic Model for Separated Turbulent Flows," AIAA Paper 78-257, Jan. 1978.

[7]Sorenson, R.L., "Three-Dimensional Elliptic Grid Generation About Fighter Aircraft for Finite-Difference Computations," NASA TM in preparation.

[8]Edwards, T.A., "Noniterative Three-Dimensional Grid Generation Using Parabolic Partial Differential Equations," AIAA Paper 85-0485, Jan. 1985.

[9]Lockman, W.K. and Seegmiller, H.L., "An Experimental Investigation of the Subcritical and Supercritical Flow About a Swept Semispan Wing," NASA TM-84367, June 1983.

[10]Holst, T.L., Thomas, S.D., Kaynak, U., Gundy, K.L., Flores, J., and Chaderjian, N.M., "Computational Aspects of Zonal Algorithms for Solving the Compressible Navier-Stokes Equations in Three Dimensions," NASA TM-86774, Oct. 1985.

[11]Van Dalsem, W.R. and Steger, J.L., "Finite-Difference Simulation of Transonic Separated Flow Using a Full-Potential Boundary-Layer Interaction Approach," AIAA Paper 83-1689, July 1983.

[12]Thibert, J.J., Grandjacques, M., and Ohman, L.H., "NACA 0012 Airfoil, An Experimental Data Base for Computer Program Assessment," AGARD-AR-138, May 1979, pp. A1-1–A1-19.

[13]Tobak, M. and Peake, D.J., "Topological Structures of Three-Dimensional Separated Flows," AIAA Paper 81-1260, June 1981.